

JGR Space Physics

RESEARCH ARTICLE

10.1029/2020JA028855

Key Points:

- Polar mesosphere summer echoes, the power of which varied on the subsecond scale, were received from the altitude of noctilucent clouds
- Pulsating aurora can modulate power of the polar mesosphere summer echo
- Meteor radar erroneously accepts variations of the polar mesosphere summer echo at subsecond scale as meteor trails

Supporting Information:

Supporting Information may be found in the online version of this article.

Correspondence to:



A. Kozlovsky,
alexander.kozlovsky@oulu.fi

Citation:

Kozlovsky, A., Shalimov, S., Lester, M., & Belova, E. (2021). Polar mesosphere summer echoes and possible signatures of pulsating aurora detected by the meteor radar. *Journal of Geophysical Research: Space Physics*, 126, e2020JA028855. <https://doi.org/10.1029/2020JA028855>

Received 22 OCT 2020
Accepted 13 OCT 2021

Polar Mesosphere Summer Echoes and Possible Signatures of Pulsating Aurora Detected by the Meteor Radar

A. Kozlovsky¹ , S. Shalimov^{2,3}, M. Lester⁴ , and E. Belova⁵

¹Sodankylä Geophysical Observatory of the University of Oulu, Sodankylä, Finland, ²Institute of Physics of the Earth, Moscow, Russia, ³Space Research Institute, Moscow, Russia, ⁴Department of Physics and Astronomy, University of Leicester, Leicester, UK, ⁵Swedish Institute of Space Physics, Kiruna, Sweden

Abstract Using data of the all-sky interferometric meteor radar (SKiYMET, 36.9 MHz) operating in the Sodankylä Geophysical Observatory (67°22'N, 26°38'E, Finland) we found a specific type of polar mesosphere summer echo (PMSE), the power of which exhibits irregular variations at a frequency of the order of a few Hz. We classified such radar echoes as pulsating PMSE. These echoes were observed in late June–July in the morning sector (4–12 MLT) during geomagnetic storms. They were received from a narrow range of altitudes near 82 km, which corresponds to the altitude of noctilucent clouds where ice particles of about 50-nm radii exist. During pulsating PMSE, the SGO ionosonde showed an electron density of the order of $3 \times 10^{11} \text{ m}^{-3}$ around 82 km, and enhanced D-region ionization was manifested in the cosmic noise absorption. We suggest that the power of PMSE is modulated by bursts of electron precipitation corresponding to the few-Hz internal modulation of pulsating aurora. During a short precipitation burst of 50–100 keV electrons, additional electrons can attach to the ice particles due to the presence of hyperthermal electrons according to the hypothesis proposed by Rosenberg et al. (2012, <https://doi.org/10.1016/j.jastp.2011.10.011>). This leads to an increase of the power of PMSE. After the burst is ended, the ice particles are deionized with a characteristic time of about 0.2 s due to attractive interaction with ions.

Plain Language Summary We present rare observations that relate to two different high-latitude phenomena, aerosol ice particles near the mesopause and pulsating aurora. Because of the global atmospheric circulation, the lowest atmospheric temperature down to about -160°C occurs in the polar mesosphere at altitudes 80–90 km during summer time. Due to this low temperature, ice aerosol particles of the size up to 50-nm exist there, which can be observed as noctilucent clouds (NLC). The ice particles can accumulate free electrons from surrounding space, so that spatial irregularities of the density of ice particles give rise to irregularities of electron density, which can be detected by radars as polar mesosphere summer echo (PMSE). In the case of pulsating aurora, the power of the PMSE detected by the radar is varying in accordance with the auroral pulsations, in spite of the aurora cannot be seen visually in the sunlight summer sky. This makes possible radar monitoring of the auroral pulsations even when visual auroral observations are impossible.

1. Introduction

Polar mesospheric summer echoes (PMSE) are a form of radar backscatter from electron density irregularities occurring in the high-latitude summer mesosphere at altitudes between 80 and 90 km, in the vicinity of the mesopause. In most cases, PMSE observations have been made with VHF (very high frequency, 30–300 MHz) radars, which implies backscatter from few meters scale irregularities. It is commonly accepted that the formation of such irregularities is associated with the ice particles existing in the cold summer mesosphere (e.g., Rapp & Lübken, 2004). Mechanisms for the formation of PMSE will be discussed in more detail in Section 4.

Almost all previous PMSE studies have been performed with a time resolution of the order of one minute to few seconds. To our knowledge, only one study using PMSE observations on the subsecond scale have been published (Sommer et al., 2016). These observations were made during two experimental campaigns, and two cases of PMSE were investigated with 2-ms temporal sampling and down to 75-m range resolutions. It

was found that the power of PMSE appears and reappears on a time scale between 0.25 and 2 s. The authors suggested that the temporal oscillation might be caused by the correlation time of the scattering process.

The time scale between 0.25 and 2 s corresponds to the lifetime of most meteor trails, so that such PMSE may be manifested in the routine data of a meteor radar operating at high latitude. Indeed, the duration of the radar echoes is a key parameter, which is used by meteor radars for identifying meteor trails. Due to this, the PMSE, the power of which varies on the subsecond scale, might be misinterpreted as scatter from meteor trails. Motivated by this, we have investigated data from the meteor radar (MR) in Sodankylä (67.4°N), which has been operating from December 2008 and, indeed, found signatures of specific PMSE (referred to below as pulsating PMSE). Having a long-term 11-year database of observations, we investigated geophysical conditions of such PMSE and their statistics. Thus, this paper may be considered as the first statistical study of PMSE on the subsecond scale.

Compared with the earlier studies where meteor radars were used to observe PMSE (e.g., Hall et al., 2020; Swarnalingam et al., 2009; Younger et al., 2021), we utilize the capability of MR signal processing to select the PMSE, the power of which varies on the subsecond scale.

In the rest of the paper, we provide parameters of the meteor radar and describe the method to identify pulsating PMSE. We then present statistics and outline features of these PMSEs. Following this, we investigate background conditions during these events, before finally discussing possible physical mechanisms for such radar echoes.

2. Instruments, Data, and Methods

2.1. Meteor Radar

The Sodankylä Geophysical Observatory (SGO geographic coordinates 67°22'N, 26°38'E, geomagnetic latitude 64°, $L = 5.25$) is located in northern Finland. The all-sky interferometric meteor radar (SKiYMET) at SGO operates at a frequency of 36.9 MHz, with a transmitted power of 15 kW. The pulse repetition frequency of MR transmissions is 2,144 Hz, but because of the coherent integration the effective sampling frequency is 536 Hz. The range resolution is 2 km. A full description of the system and principles of operation can be found in Hocking et al. (2001). The SGO radar has operated permanently since December 2008, although due to repair there were two important breaks during July 17 to August 01, 2017 and July 12 to August 02, 2018.

The SKiYMET radar software includes a data analysis algorithm for selecting backscatter from meteor trails while at the same time rejecting other signals such as, e.g., echoes from aircrafts or lightning. The characteristic features used to distinguish meteor echoes from other signals include their rapid onset, relatively short duration (typically <1 s), and quasiexponential decay. In routine MR operation for each echo accepted as a meteor (i.e., “detection”) short 4-s records of the signals (real and imaginary components) received at each of the five antennas are analyzed and archived. A typical example of such a record of a detected meteor is shown in Figure 1a, where the amplitude of the signal received at one of the antennas is presented versus time (zero time corresponds to the time of meteor detection obtained in the routine MR operation). Effectively the meteor selection procedure works like a band-pass filter accepting the echoes, the power of which is changing at the subsecond scale (at a frequency of a few Hz). Certain nonmeteor signals may be accepted, however, and subsequently treated as meteors as well. For instance, there can be radar reflections similar to those caused by meteor trails that are caused by fluctuating auroral precipitation (Kozlovsky et al., 2019) or the remains of rocket fuel (aerosol particles) (Kozlovsky et al., 2017). By assuming that radar echoes from pulsating PMSE might be mistakenly identified as echoes from meteor trails by the SKiYMET radar, we have investigated carefully the parameters of the meteor radar detections.

For the targets detected by the radar, their direction (azimuth and elevation angles), range, the Doppler velocity of the scatter from these targets, and the decay time of the scatter from the targets (i.e., the time for which the amplitude of the backscattered signal falls to one half of its maximum value) are routinely determined. The line-of-sight drift speed and positions of the meteor trails are used to deduce the horizontal wind velocity at altitudes of 80–100 km. In the standard mode the time and height resolution of the wind data are 1 h and 2–3 km, respectively.

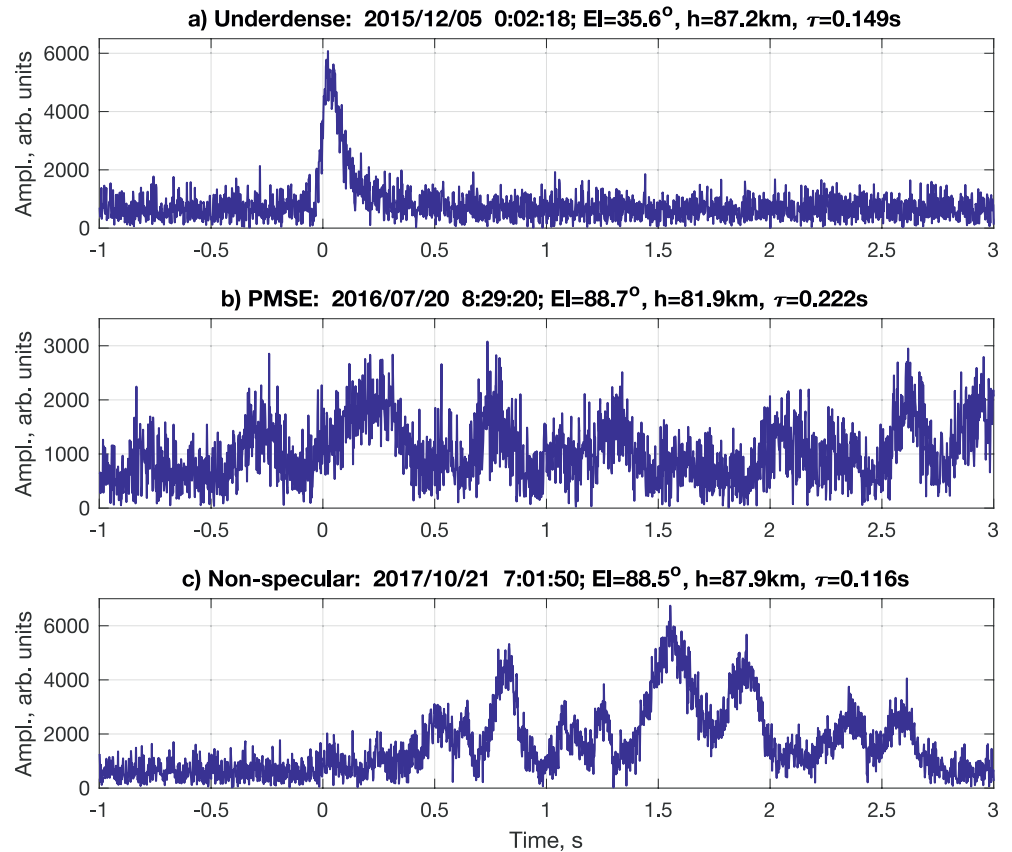


Figure 1. The amplitude of the signals received at one of the five meteor radar antennas versus time (zero time approximately corresponds to the time of meteor detection in routine meteor radar operation): (a) a typical example of meteor detection; (b) an example of polar mesosphere summer echo (PMSE) detected near zenith; (c) nonspecular meteor echo detected near zenith.

2.2. Near-Zenith Echoes

The meteor radar accepts echoes from cylindrical meteor trails in the cases when the wave vector is perpendicular to the trails (i.e., specular reflection occurs). Because of this, meteor trails are very seldom detected at high elevation angles. Indeed, for a near-zenith detection, the trail should be parallel to the Earth's surface, but in such a case the meteor would burn out far away from the radar zenith. PMSE, on the other hand, are well detected at high elevation angles. We have, therefore, used this characteristic to search for signs of PMSE in the meteor radar data.

We have selected all detections at elevation angles higher than 83° (referred to subsequently as near-zenith or NZ detections) and counted the number of such detections for every day from December 2008 to August 2019. These data are presented in Figure 2. In most days, only a few (<20) near-zenith detections have been obtained, but some days show outstanding peaks of up to several tens of such detections. We have carefully looked through the radar data from these days.

In most cases, large daily numbers of near-zenith detections were obtained during peaks of major meteor showers such as the Geminids (December 13–14), Quadrantids (January 03), Perseids (August 11–14), Orionids (October 21–22), and others. As an example, Figure 3 presents the key parameters, elevation angle (panel a), height (panel b), and line-of-sight velocity (panel c), of the MR detections as a function of UT on October 21, 2017 when 23 NZ echoes were received during the Orionids meteor shower. Red dots indicate near-zenith detections. The NZ targets were located at different heights between 85 and 110 km. In some cases, several NZ targets were detected almost simultaneously at different heights. For instance, during two seconds between 07:51:46 and 07:51:48 UT, there were four NZ detections at descending heights from

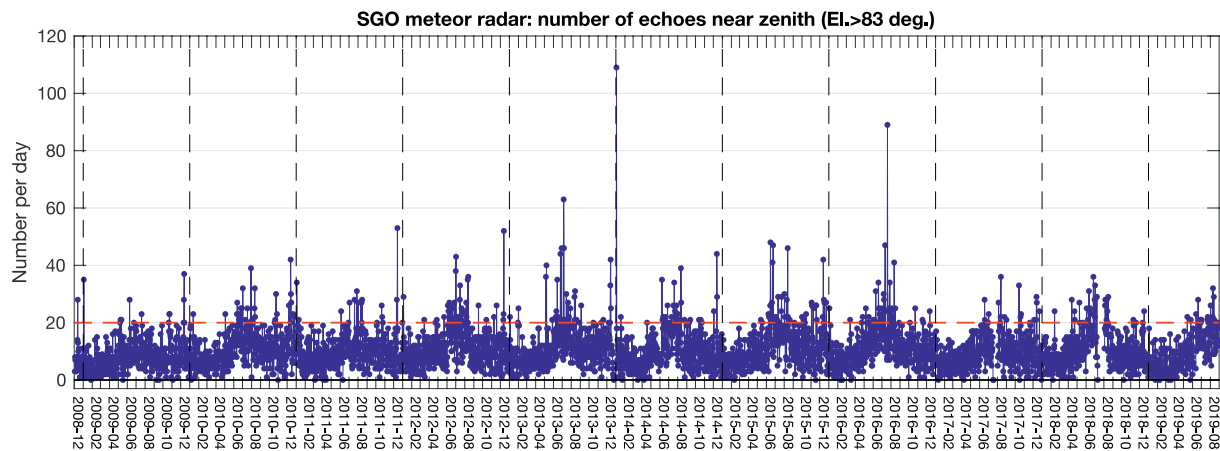


Figure 2. The daily number of meteor radar detections at elevation angles higher than 83° (near-zenith detections).

107 km down to 99 km. Such multiple echoes are typically received from the electron density irregularities generated due to turbulence along tracks of relatively large meteoroids (Kozlovsky et al., 2018, 2020). This phenomenon is known as nonspecular reflection from nonfield-aligned irregularities formed along meteor trails, which was explained by the presence of charged dust forming from the meteoric material immersed in a turbulent flow (Chau et al., 2014). For these radar reflections, the radar wave vector is not necessarily perpendicular to the trails of meteors, such that echoes at high elevation are possible for the meteors occurring near the zenith of MR independently of the directions of their trajectories. An increased number of bright meteors (large meteoroids) occurs during major meteor showers, which causes a larger number of the nonspecular echoes detected near zenith. In the present study, we abandon such cases.

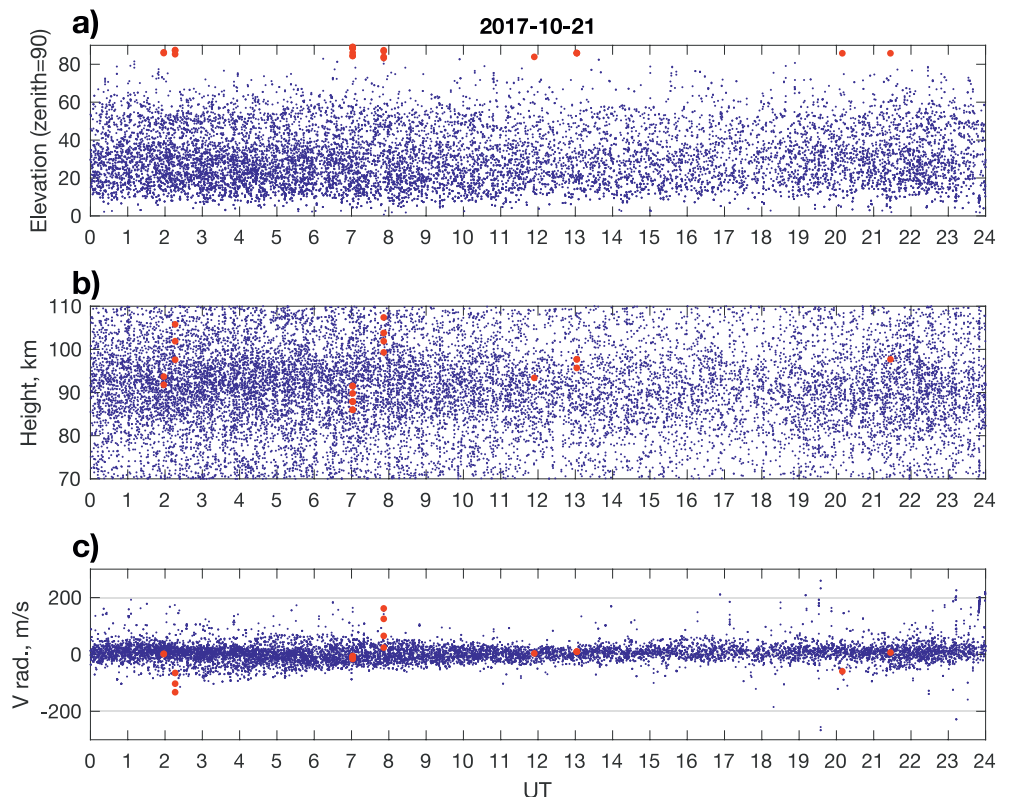


Figure 3. The key parameters of meteor radar detections during peak of Orionids on October 21, 2017: (a) elevation angle; (b) height; (c) line-of-sight velocity. Red dots indicate near-zenith detections.

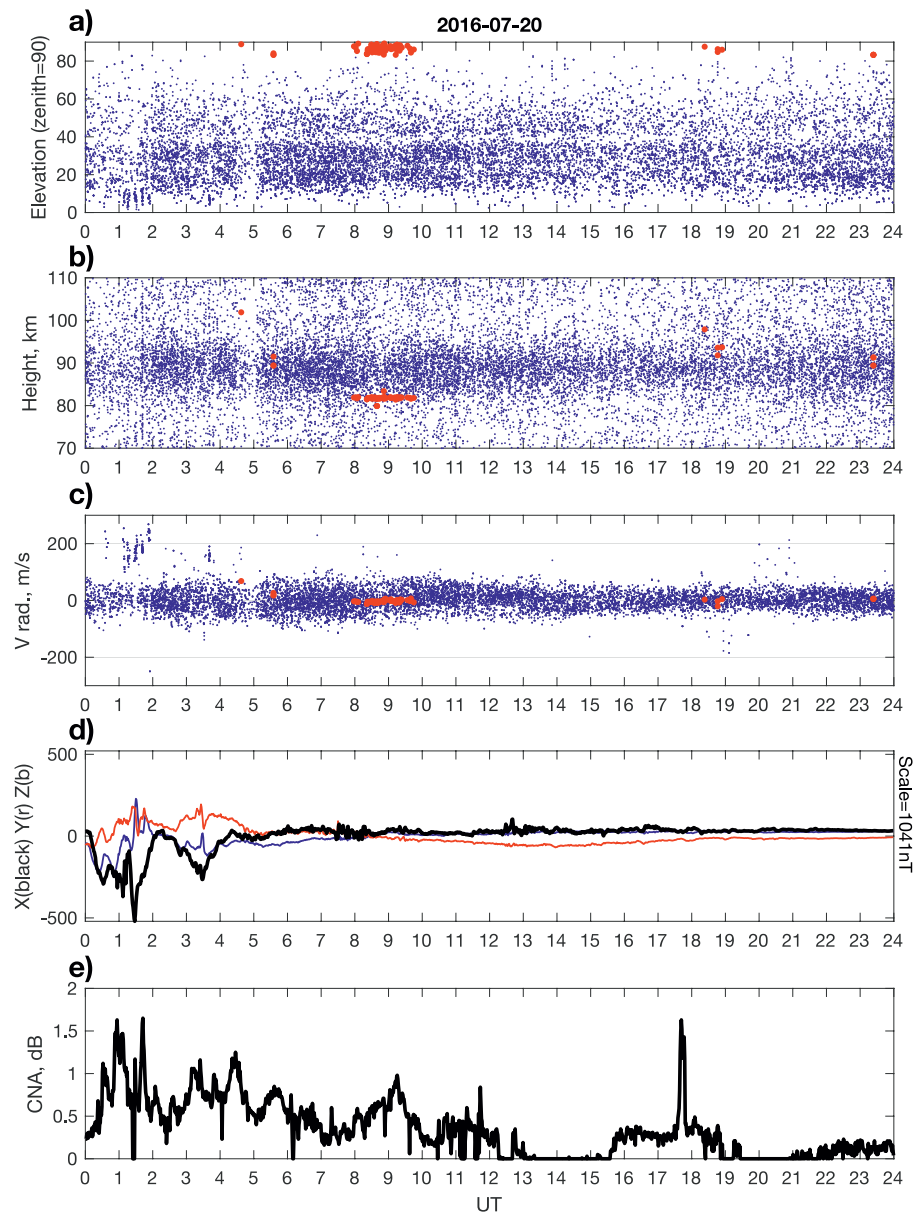


Figure 4. The key parameters of meteor radar detections and geophysical conditions during polar mesosphere summer echo (PMSE) event on July 20, 2016: (a) elevation angle, (b) height, and (c) line-of-sight velocity of meteor radar targets (red dots indicate near-zenith detections); (d) three components of geomagnetic field at Sodankylä Geophysical Observatory (SGO); (e) cosmic noise absorption at SGO.

In other cases, the increase of daily number of NZ echoes was not associated with peaks of meteor showers. A typical example of MR data on such a day is presented in Figure 4 where the three top panels again show the elevation angle, height, and line-of-sight velocity of targets, and the red dots indicate near-zenith detections, following a similar format as in Figure 3. Altogether there were 89 NZ echoes and the great majority of them were obtained from the same height near 80 km. This case took place in summer, on July 20, 2016, so that we may suspect that these echoes might be PMSEs. In comparison with the meteor NZ echoes detected throughout a day (or a large part of the day), the PMSE related NZ echoes were concentrated in relatively short time intervals of the order of 1–2 h. For instance, in the case presented in Figure 4, the echoes were detected during 2 h between 8 and 10 UT. We have used this feature to search for possible PMSE echoes in the radar data.

Table 1

Parameters of the Events: Date, Time, Number of NZ Echoes, Doppler Velocity, and Decay Time; Solar Wind Velocity and Dynamic Pressure; Geomagnetic Indices: *Dst* and *ap*; Cosmic Noise Absorption at SGO; Characteristics of Geomagnetic Storms: Trigger, Start Day, and Minimum *Dst*

Date	Time UT (MLT \approx UT + 3)	<i>N</i>	<i>H</i> (km)	<i>V</i> (m/s + away)	τ (s)	V_{sw} (km/s)	<i>Psw</i> (nPa)	<i>Dst</i> (nT)	<i>ap</i> (nT)	CNA (dB)	Solar wind	Start	Min <i>Dst</i>
July 01, 2012	01:53–02:24	30	82.0 \pm 0.7	2.0 \pm 3.5	0.26 \pm 0.18	651	3.3	–17	22	2.0	HSS	June 30	–37
July 02, 2012	05:10–06:18	26	81.9 \pm 0.3	0.4 \pm 3.0	0.30 \pm 0.19	650	2.6	–32	27	2.2	HSS	June 30	–37
July 09, 2012	04:15–04:47	11	83.8 \pm 0.1	–1.1 \pm 6.0	0.22 \pm 0.16	419	1.3	–33	22	0.8	CME	July 08	–78
June 25, 2013	03:27–04:34	18	81.9 \pm 0.9	–4.2 \pm 3.9	0.37 \pm 0.18	532	1.0	–35	9	0.9	HSS	June 20	–49
June 29, 2013	03:22–08:50	41	82.5 \pm 2.6	–3.2 \pm 6.9	0.30 \pm 0.18	372	1.7–4.4	–99	80	2.9	CME	June 28	–102
July 06, 2013	05:00–06:22	41	82.8 \pm 2.2	–2.4 \pm 4.7	0.32 \pm 0.21	360	1.3	–63	32	2.3	SI	July 05	–87
July 07, 2013	00:59–01:59	27	82.1 \pm 1.8	0.5 \pm 4.0	0.27 \pm 0.16	321	1.1	–47	27	1.9	SI	July 05	–87
July 15, 2013	04:16–04:50	18	81.0 \pm 1.0	–5.3 \pm 2.9	0.28 \pm 0.18	377	3.4	–50	48	3.0	CME	July 13	–81
June 24, 2015	04:23–04:48	15	82.5 \pm 0.9	–3.5 \pm 1.6	0.16 \pm 0.04	586	1.0	–83	18	1.7	CME	June 22	–204
July 12, 2016	04:14–07:42	41	82.5 \pm 1.1	–4.1 \pm 3.0	0.25 \pm 0.11	512	2.4	–22	32	2.9	HSS	July 08	–31
July 20, 2016	08:01–09:46	76	81.7 \pm 0.4	–3.5 \pm 4.1	0.37 \pm 0.17	565	6.6–7.7	–12	15	1.0	CME	July 20	–23
June 26, 2018	02:35–03:00	13	82.5 \pm 2.8	–10.1 \pm 7.0	0.34 \pm 0.14	406	5.6	–41	39	4.2	CME	July 25	–48
June 24–July 20	00:59–09:46	$\Sigma = 357$	82.2 \pm 1.6	–2.6 \pm 5.0	0.30 \pm 0.17								
Cases from Sommer et al. (2016)													
June 20, 2014	06:30–07:50		82–83			428	1.5–2.0	–8	9		SI	June 18	–34
June 09, 2015	00:00–07:00		82–84			620	2.3–3.0	–35	15–22		HSS	June 08	–73

We have selected all cases when >10 NZ echoes were obtained during 1 h. Altogether, there were 34 days when such cases occurred. Out of them, 22 days coincided with major meteor showers. The MR data for these days are similar to that shown in Figure 3, namely there are simultaneous echoes from different heights indicating nonspecular trails associated with bright meteors. We do not, therefore, consider these events in the present paper.

The meteor radar data in the remaining 12 days are similar to that presented in Figure 4. These data are presented in Figures S1–S12 in Supporting Information S1, and in the following we focus on these events. Thus, from 11 years of the observations, we have selected the intervals when, first, >10 echoes during 1 h were received at high elevation (higher than 83°) and, second, these echoes apparently were not associated with meteors. Altogether, there were 12 such cases.

3. Results

Table 1 contains the dates and time of the selected events, the number of NZ echoes, and the mean parameters of the echoes, such as height, the Doppler velocity, and the decay time. Two features can be seen here. First, all the events occurred between June 24 and July 20, which coincides with the deep minimum of temperature at 80–100 km over Sodankylä (Lukianova et al., 2018), and this time interval corresponds to the annual peak of PMSE occurrence (Smirnova et al., 2010). Second, the NZ echoes were located at heights near 82 km, and this is within the typical height interval of PMSE between 80 and 90 km (Rapp & Lübken, 2004). For these two reasons, we may suspect that the observed events belong to PMSE. In the following, we present information on the shape of the received NZ signals during the selected events.

3.1. Shape of the Summer Near-Zenith Echoes

Figure 1b presents an example of a near-zenith echo during the event on July 20, 2016. The echo was received at an elevation of 88.7° from a height of about 82 km. The amplitude of the signal (i.e., voltage at a receiving antenna) shows irregular, quasiperiodic variations, such that the shape of the signal is clearly different from that of a meteor detection (e.g., Figure 1a). In the MR signal processing, the decay time of the

signal (τ) was determined as 0.222 s. This time is calculated from the width of the autocorrelation function. For an underdense meteor trail, it corresponds to the time for which the amplitude of the backscattered signal falls to one half of its maximum value, whereas for a sinusoidal signal, it would be equal to a half period of the oscillations, i.e., for a quasisinusoidal signal $T \approx 2\tau$.

We note here that if the amplitude of a received signal has a sinusoidal shape, then the period of modulation must be shorter than about 0.6 s (frequency higher than 1.7 Hz) to be accepted by the routine processing in the radar as a meteor echo. Otherwise, the growth time of the signal is longer than 0.3 s, and such a signal is treated as a nonmeteor echo (Hocking et al., 2001). Also, slowly decaying signals are rejected, such that in practice only signals with the characteristic time shorter than about 1 s (periodicity shorter than 2 s) are accepted. This feature is important for interpreting the meteor radar data in the present study.

The 4-s records of the signals of the other NZ detections were obtained, although the data were lost for 7 out of 12 events (the years 2013, 2015, and for July 2, 2012). For the remaining five events, the data are presented in Figures 5a–5e as a color-coded plot showing the amplitudes of the NZ echoes detected during the events as a function of the record duration time (horizontal axis) and the time of detection (vertical axis, the scale is not uniform). This figure shows that the power of the signals appears and reappears on a time scale of the order of 0.5 s, which is very similar to the PMSE observations by Sommer et al. (2016).

Taking into account the shape of signals, the time of occurrence (between June 24 and July 20), and the height of the echoes (near 82 km), we conclude that the observed events belong to PMSE. However, these events are extremely rare (only 12 1-h events during 11 years), whereas at such latitudes the occurrence rate of PMSE detected in the usual manner between late May and late August is about 70% (Smirnova et al., 2010). Hence, the phenomenon we have observed should be classified as a specific type of PMSE. An important peculiarity of these radar echoes is the subsecond variations of their amplitude, and we, therefore, specify them as “pulsating PMSE.”

For comparison, Figure 1c shows an example of a nonspecular meteor echo during the Orionids meteor shower on October 21, 2017, and Figure 5f presents all the 4-s records of the NZ echoes detected on this day. Unlike the PMSE related echoes, the meteor echoes are characterized by a sharp increase of the amplitude of the return at the moment of meteor entry, and their amplitudes are essentially larger than that of PMSE. Such echoes have been studied in (Kozlovsky et al., 2018, 2020).

3.2. Statistical Characteristics of Pulsating PMSE

Altogether, there were 357 NZ echoes detected during the 12 selected PMSE events. Their statistical characteristics are presented in Figure 6 as histograms showing height (a), decay time (b), and magnetic local time (c) distributions of the echoes.

The histogram in Figure 6a shows the height distribution of the NZ echoes. A sharp peak indicates that the majority of the echoes (72%) were obtained from the height 82 ± 0.5 km. This corresponds to the altitude of noctilucent clouds (NLC) where the largest ice particles (~ 50 nm in radii) exist (von Cossart et al., 1999). Being formed near the point with coldest temperatures (mesopause, at about 88 km), the ice particles sediment and grow, down to about 82 km where they can be optically observed as NLC. Below this altitude, the ice particles melt.

Figure 6b presents the line-of-sight velocity of the radar echoes. Predominantly, the velocity of pulsating PMSE was a few m/s or near zero (see also Table 1). Such velocity values may be explained by a contribution from the horizontal wind or/and an enhancement of the vertical wind, whereas the velocity of the ice particles' sedimentation by gravity may be as small as a few cm/s (e.g., Gudadze et al., 2019; Reid, 1975). The velocity of the horizontal wind at 82 km deduced from the SGO meteor radar during the PMSE events is given in Table S1 in Supporting Information S1. Typically, the velocity was 50–70 m/s, which would provide a line-of-sight velocity of a few m/s at the given elevations.

Figure 6c presents the distribution of the decay time of the echoes. The decay time varied between 0.1 and 0.7 s, which corresponds to periods of fluctuations between 0.2 and 1.4 s (frequency range 0.7–5 Hz) with the maximal occurrence at about 0.4 s (2.5 Hz).

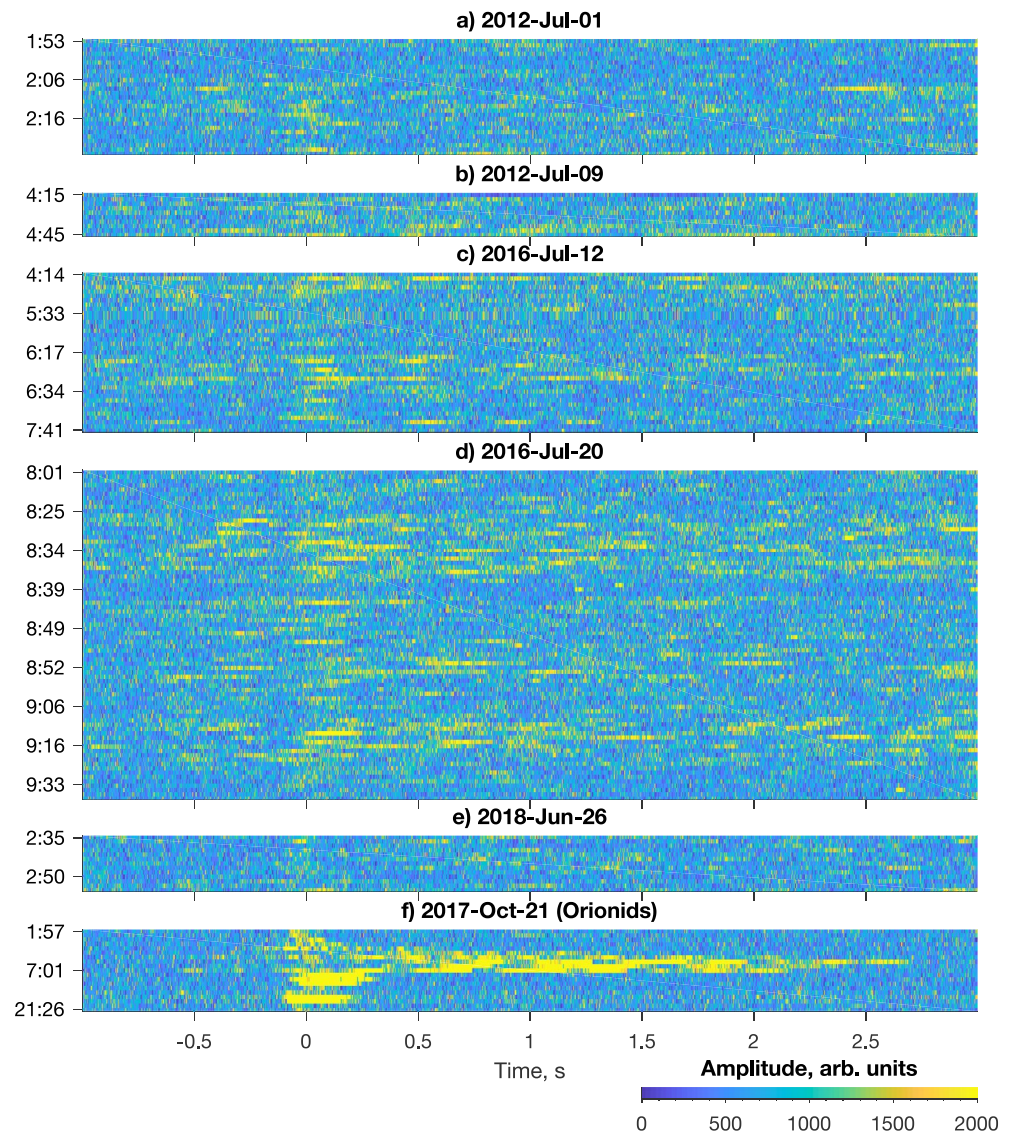


Figure 5. Color-coded plots showing amplitudes of the near-zenith echoes as functions of the record duration time (horizontal axis, zero time approximately corresponds to the time of meteor detection in routine meteor radar operation) and time of detection (vertical axis, the scale is not uniform): (a–e) echoes detected during polar mesosphere summer echo (PMSE) events; (f) nonspecular meteor echoes during Orionids on October 21, 2017.

Figure 6d shows the distribution of the PMSE with magnetic local time. All the events were observed between 04 and 13 MLT (approximately equivalent to 01 and 10 UT) with maximal occurrence around 09 MLT. This is the morning sector, which is characterized by precipitation of energetic electrons (few tens keV) at the latitude of SGO. Such electrons produce ionization in the ionospheric D-layer below 90 km and, hence, may influence the radar backscatter at the height of PMSE. Indeed, enhanced D-layer ionization was manifested in the cosmic noise absorption (CNA) observed at SGO during the events. For instance, a CNA enhancement up to about 1 dB during the event between 08 and 10 UT on July 20, 2016 is shown in Figure 4e. Similar data for the other events are presented in Figures S1–S12 in Supporting Information S1 and summarized in Table 1. During all the events enhanced cosmic noise absorption (CNA) of the order of 1–4 dB was recorded at SGO, which indicates electron precipitation in the D-layer. Enhanced D-layer ionization was also observed in the data of SGO ionosonde. For example, the ionogram taken at 08:15 UT on July 20, 2016 (Figure 7) shows the ionosonde reflection from the height 82 km at frequencies up to 5 MHz, which

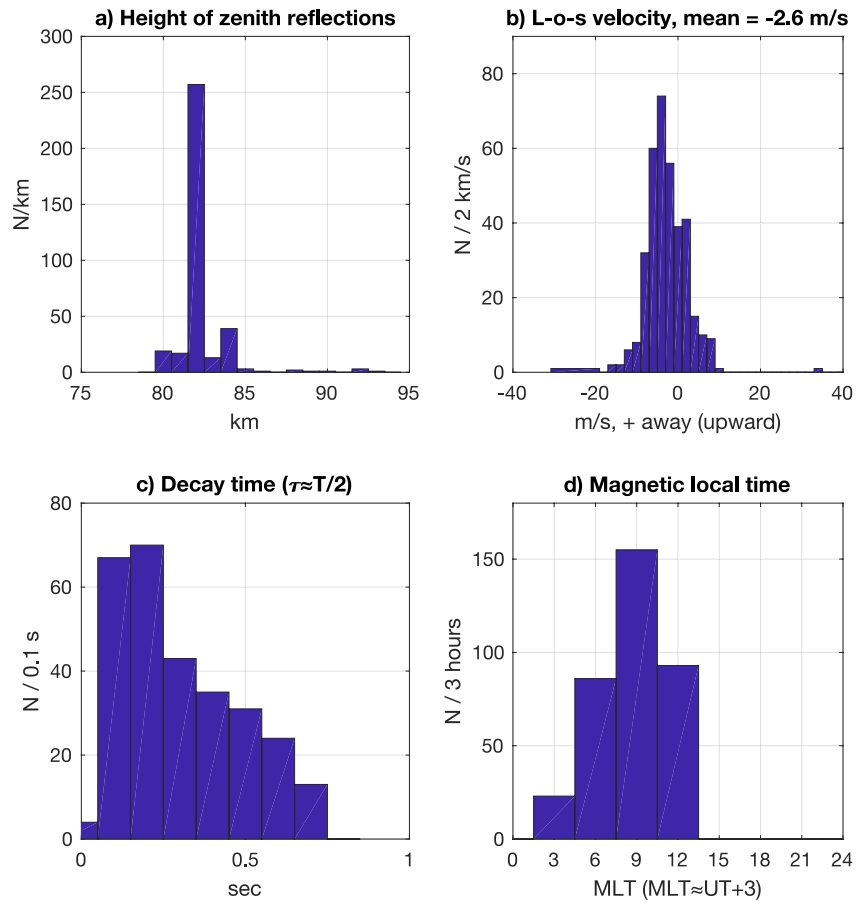


Figure 6. Histograms showing statistical characteristics of near-zenith echoes detected during selected polar mesosphere summer echo (PMSE) events: (a) height, (b) the line-of-sight velocity, (c) decay time, and (d) magnetic local time distributions of the echoes.

corresponds to an electron density $3 \times 10^{11} \text{ m}^{-3}$. The electron precipitation depends on magnetospheric disturbances, and, therefore, in the following, we consider the geophysical conditions during the events.

3.3. Geophysical Conditions

Figure 4d shows variations of the three components of geomagnetic field observed at SGO on July 20, 2016. It was a disturbed day, and negative geomagnetic disturbances in the H-component of the order of 500 nT indicating a substorm activity occurred before the events of pulsating PMSE. The data of geomagnetic field for the other events are presented in Figures S1–S12 in Supporting Information S1. For all the pulsating PMSE events, geomagnetic disturbances of the order of few hundreds nT were recorded at SGO before or during the events.

Table 1 presents the parameters of the solar wind (speed, V_{sw} , and dynamic pressure, P_{sw}) and indices of geomagnetic activity (Dst and ap) during the events (averages over the period during the observation of the echoes). These data were obtained from the OMNI database (King & Papitashvili, 2005). One can see that all the events occurred under disturbed geomagnetic conditions characterized by negative Dst and enhanced ap values.

Two events on July 01 and 02, 2012 occurred during a weak geomagnetic storm with minimum $Dst = -37 \text{ nT}$. This storm started on June 30 and was caused by the solar wind High-Speed Stream (HSS) identified in the catalog of Grandin et al. (2019). The solar wind speed was enhanced up to 650 km/s. Characteristics of the storm (start date and minimum Dst) and the solar wind features (HSS) are given in Table 1. Moreover, two

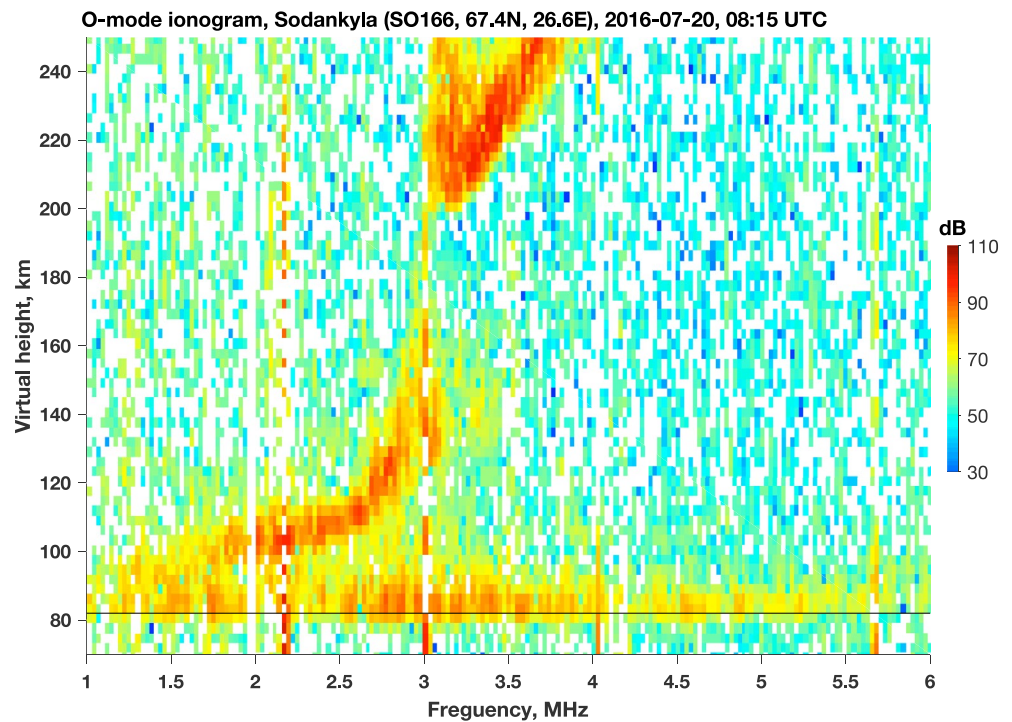


Figure 7. The Sodankylä Geophysical Observatory (SGO) ionogram at 08:15 UT on July 20, 2016. The horizontal black line indicates 82-km height.

other events, on June 25, 2013 and July 12, 2016, occurred during weak geomagnetic storms (minimum Dst between -30 and -50 nT) associated with HSS identified in the same catalog (Grandin et al., 2019).

Six events in the list were associated with geomagnetic disturbances caused by near-Earth interplanetary Coronal Mass Ejections (CME), according to the catalog provided by Richardson and Cane (2010), which covers the years from 1996 onward and is regularly updated (<http://www.srl.caltech.edu/ACE/ASC/DATA/level3/icmetable2.htm>). Two events, on June 29, 2013 and June 24, 2016, occurred during intense geomagnetic storms ($Dst < -100$ nT) which started one-two days before (on June 28, 2013 and June 22, 2016, respectively). In the other cases, there were moderate (-100 nT $< Dst < -50$ nT) on July 09, 2012 and July 15, 2013, or weak ($Dst > -50$ nT) on July 20, 2016 and July 26, 2018 geomagnetic storms.

Two events, on July 06 and 07 were associated with a moderate geomagnetic storm (minimum $Dst = -87$ nT) that started on July 05. In this case, neither CME nor HSS were indicated in the catalogs, but there was a sudden impulse (SI) in the solar wind pressure up to 5.4 nPa just before the storm onset, which can be considered as a trigger of the storm.

Thus, in all the cases, pulsating PMSE occurred during geomagnetic storms. Moreover, the two cases described by Sommer et al. (2016) also took place during weak (June 20, 2014) or moderate (June 09, 2015) geomagnetic storms caused by an SI and an HSS, respectively. The same parameters of these events as for those discussed here are given at the bottom of Table 1. In both cases, the radar echoes were received in the morning sector from heights between 82 and 84 km. We believe, therefore, that these echoes can be classified as pulsating PMSE, the same as these described in the present study.

3.4. Evidence for Presence of Ice Particles

As additional check for the presence of the ice particles, we have looked through data of the ESRAD VHF radar (ESRAD) located in northern Sweden (67.88°N , 21.10°E), near Kiruna, about 240 km west of Sodankylä. ESRAD is a mesosphere-stratosphere-troposphere (MST) radar operating at a frequency of 52 MHz. A detailed description of the radar is given in Chilson et al. (1999).

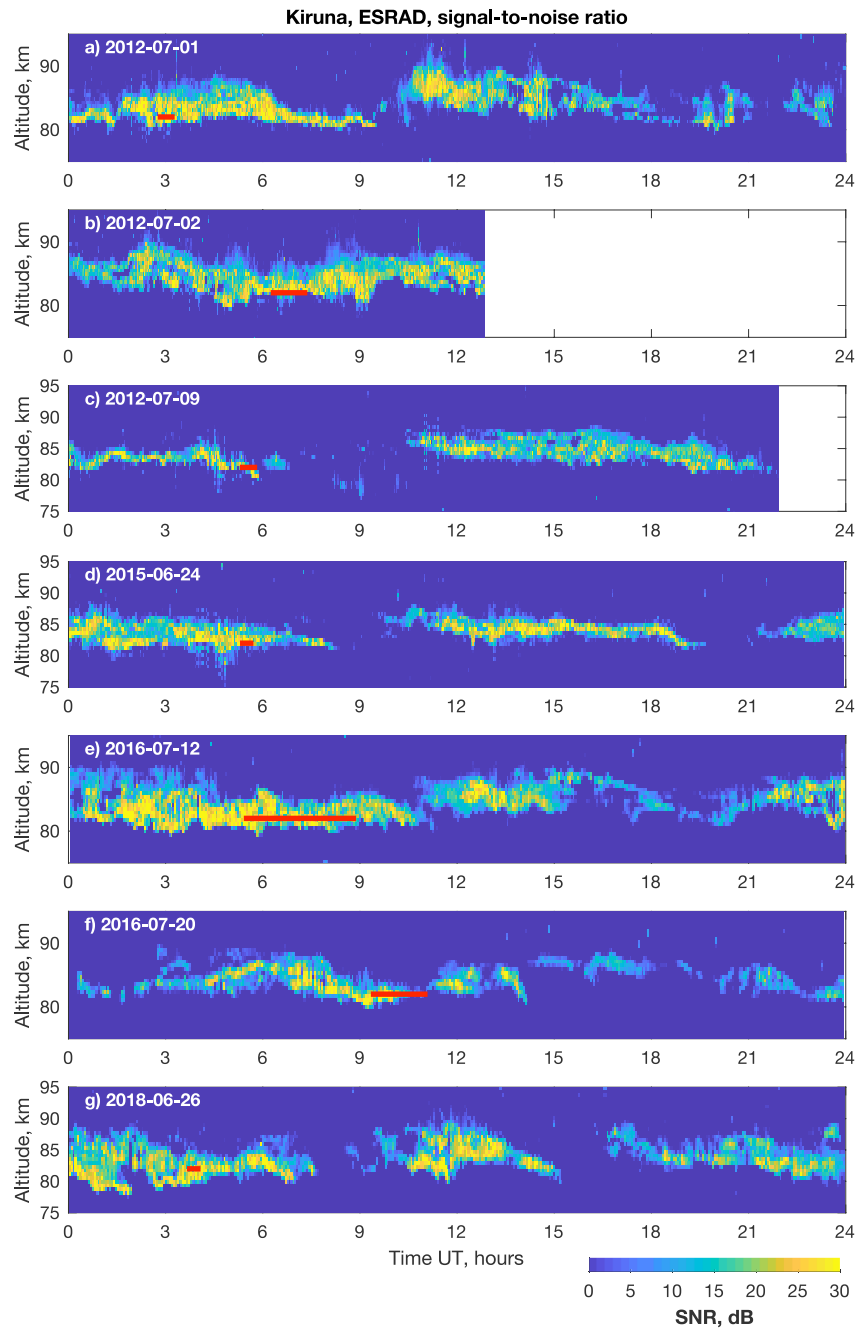


Figure 8. Backscatter power measured with the ESRAD mesosphere-stratosphere-troposphere (MST) radar in Kiruna during the pulsating polar mesosphere summer echo (PMSE) events. Color scale indicates a signal-to-noise ratio (dB). Red lines near the altitude of 82 km correspond to the time of pulsating PMSE in Sodankylä, with the time shift for the horizontal wind.

Data from the ESRAD radar exist for seven cases of pulsating PMSE (in the other five cases, the radar was no operational at the time of these events). Figure 8 shows the ESRAD data as daily plots of a signal-to-noise ratio of the backscatter from 75-km to 95-km altitudes. Following Kaifler et al. (2018) who used remote MST radar data to show the presence of ice particles at a given location, we utilized data of the neutral wind (Table S1 in Supporting Information S1) to estimate the transport time of ice particles from the location of the meteor radar to the location of the ESRAD radar. The wind at the altitude of 82 km was predominantly westward, 40–70 m/s. Taking into account the transport time (about 1 h), we have indicated the intervals

corresponding to the events of pulsating PMSE in Sodankylä by the red lines near 82-km altitude in Figure 8. In all the cases, the ESRAD radar detected PMSE at this altitude in the given time, which confirm the presence of ice particles during pulsating PMSE.

4. Discussion and Interpretation

The main findings of the present study can be formulated as follows. In the summer time (late June–July), the SGO VHF meteor radar at high latitudes (around 67°N) sometimes detects near-zenith echoes in a very narrow interval of altitudes near 82 km. The echoes occur in the morning sector (4–12 MLT) during geomagnetic storms. The Doppler velocity of the echoes is a few m/s or near zero. The amplitude of the echoes shows irregular variations at frequencies of a few Hz, such that we classified these echoes as pulsating PMSE. The pulsating PMSE were observed as events lasting about 1–2 h when >10 near-zenith echoes per an hour were detected. During 11 years of observations there were as few as 12 events recorded. The height of the echoes, 82 km, corresponds to the altitude of NLC, which is in the lowest part of the typical PMSE height distribution having a maximum near 85 km.

According to the standard scenario (Rapp & Lübken, 2004), the altitude range between 80 and 90 km in the summer polar mesopause region is the place where ice particles exist. Being formed near the point with the coldest temperatures (around 88 km), the ice particles sediment and grow down to the NLC altitudes at about 82 km, where their radii have become as large as about 50 nm. Below 82 km the ice is melting. Turbulent flows caused by the dissipation of atmospheric gravity can transport the ice particles. As a result, the turbulent velocity field leads to spatial irregularities in the concentration of the ice particles. As far as these ice particles are immersed in the plasma of the D-region, electrons attach to the ice surfaces such that the particles become charged and the density of free electrons decreases in the places where the ice particles are concentrated. Thus, irregularities in the density of ice particles give rise to irregularities in the electron density. The electron density irregularities with a spatial scale at half the radar wavelength are able to backscatter the radar signal, which is observed as PMSE. The power of the radar backscatter depends on the gradient of electron density, which is related to the gradient of $n_a Z_a$ where n_a is the density of the ice particles and Z_a is the number of electrons attached to a single ice particle.

A mysterious feature of the pulsating PMSE is the amplitude variations at a frequency of the order of a few Hz. Sommer et al. (2016), who were the first to notice this phenomenon, suggested that the variations are caused by the correlation time of the scattering process. They attributed the correlation time to the neutral air turbulence or influence of infrasound, in which cases the variations of the power of radar return are due to interference of reflections from numerous irregularities moving in different directions within the scattering volume. However, this scenario does not explain why the pulsating PMSE are so rare, why they are detected exclusively during geomagnetic disturbances, and why they occur in the morning sector.

Alternatively, the few-Hz pulsations may be caused by temporal variations of irregularities, rather than their motion. In the following, we consider this alternative hypothesis. Remarkably, all the cases of pulsating PMSE were observed in the morning sector at auroral latitudes during geomagnetic disturbances. Such a location and conditions are favorable for pulsating aurora (Kvifte & Pettersen, 1969). Pulsating aurora is characterized by a quasiperiodic auroral emission exhibiting a wide range of time periods from 1.6 to 15 s, and an internal modulation in the frequency range from 1.5 to 3.3 Hz is embedded in the main pulsations (Nishiyama et al., 2014). This frequency range corresponds to the frequency of pulsating PMSE, so that it is reasonable to consider the possibility that pulsating aurora modulates the intensity of PMSE.

Pulsating aurora is caused by the precipitation of electrons in an energy range from tens keV up to at least 200 keV (Miyoshi et al., 2015). Indeed, evidence of high-energy electron precipitation was observed in the data of CNA during all events of pulsating PMSE discussed here. Moreover, the SGO ionosonde data showed enhanced electron density at the PMSE height near 82 km, which corresponds to the energy of precipitating electrons in the range between 50 and 100 keV (Rees, 1963). The next question is whether the tens-keV electron precipitation pulsating at subsecond time scale can modulate the power of PMSE by affecting the charge of ice particles at 82-km height.

To answer the above question, in Appendix A, we have estimated the charge number (Z_a) of ice particles and the time constants of electron capture and deionization of them for typical undisturbed conditions and conditions of pulsating PMSE. The pulsating PMSE were obtained from the height around 82 km, which corresponds to the altitude of NLC where the largest ice particles (~ 50 nm in radii) exist (e.g., von Cosart et al., 1999). Ice particles of this size may carry 1–2 electrons during undisturbed conditions, whereas during auroral precipitation this number may increase up to about four electrons due to the presence of hyperthermal electrons according to the hypothesis suggested by Rosenberg et al. (2012). For ice particles of this size, the time of electron attachment to them during precipitation is about 0.01 s (Equation A3). After the precipitation is ended, the time of deionization of the particles due to attractive interaction with ions is about 0.2 s (Equation A5). These estimates allow the following scenario for the cause of pulsating PMSE.

Prior to the pulse of precipitation, irregularities of the ice particle density and corresponding irregularities of electron concentration exist in the range of altitudes between 80 and 88 km, which is manifested as “usual” PMSE observed by ESRAD (Figure 8). The power of these PMSE is nearly constant therefore the meteor radar does not accept these echoes as meteors. At that time, the ice particles are charged according to Equation A2. In particular, 50-nm particles carry about two electrons.

Pulsating precipitation corresponding to the internal modulation can be represented as short (0.2–0.5 s) periodically repeating bursts of 50–100 keV electrons precipitating to the height of NLC. In response to the precipitation the ice particles can quickly, during 0.01 s, accumulate additional electrons due to the presence of hyperthermal electrons according to Equation A3. The largest 50-nm ice particles attributed with lower part of NLCs near 82 km can accumulate up to four electrons, i.e., twice as much than before. This should increase the power of the radar backscatter.

When the precipitation burst is ended, the hyperthermal electrons are thermalized for the time < 0.01 s (Equation A4). After that the ice particles lose their excessive charge due to attractive interaction with ions. According to Equation A5 for 50-nm particles the time constant of deionization is 0.2 s.

Thus, we obtain fast (0.2–0.5 s) growing and fast (of the order of 0.2 s) decaying amplitude of PMSE backscatter, which is erroneously recorded by the meteor radar as a meteor trail. Such a variation of the amplitude of MR return corresponds to the example of pulsating PMSE in Figure 1b at about 0–0.5 s.

In this scenario, large ice particles play a key role. According to Equation A5, for fast deionization at subsecond time scale large ice particles, with a radius of order 50 nm, are required. Also, larger particles are able to attach more electrons, which increases the power of pulsating PMSE. This can explain that pulsating PMSE occur at the height 82 km because the largest ice particles exist there, and that these PMSE are observed in late June–July because of the lowest mesospheric temperature (100–120 K) at the given location (Lukianova et al., 2018).

Beside the size of the ice particles, the other important parameter is the electron density at PMSE height. The times of deionization (Equation A5) is shorter for larger electron density, such that a high enough electron density is necessary for the proposed mechanism of pulsating PMSE. On the other hand, high electron density indicates strong electron precipitation, which is necessary for producing the population of hyperthermal electrons. In certain cases, the SGO ionosonde showed an electron density $(2\text{--}4) \times 10^{11} \text{ m}^{-3}$ during pulsating PMSE, and we used such a value for numerical estimations. However, in other cases, blackout of the ionosonde occurred, i.e., the ionosonde signal was totally absorbed because of high electron density in D-region. Moreover, due to the absorption, the meteor radar echoes may be essentially attenuated when the D-layer electron density is too high. For instance, in the case shown in Figure 4, there was enhanced absorption between 4 and 5 UT, which caused a lowering of the meteor count. Thus, although intense precipitation of tens-keV electrons is necessary for pulsating PMSE, too strong precipitation can make the radar observations impossible because of D-region absorption, so that there is a range of electron flux intensities within which pulsating PMSE may be observed.

Ice particles as large as 50-nm exist only in the lowest part of the PMSE layer, and the electron density in D-layer is usually $< 10^{11} \text{ m}^{-3}$. For more common conditions (e.g., 20-nm ice particles and an electron density $10^9\text{--}10^{10} \text{ m}^{-3}$) the characteristic time according to Equation A5 is one to a few minutes, which is too long to respond to electron precipitation with a period of order of a few Hz.

In the suggested mechanism for the SKiYMET detection of pulsating PMSE a coincidence of a number of specific conditions is required, namely, large 50-nm ice particles in the mesosphere, few-Hz pulsating electron precipitation, energy of precipitating electrons 50–100 keV, and electron flux of certain intensity to produce D-region ionization of the order of $(2\text{--}4) \times 10^{11} \text{ m}^{-3}$. Such a coincidence of factors is rare, and hence the reason why pulsating PMSE are so rare.

One should remember that pulsating PMSE in the present study were detected in the standard meteor radar operational mode designed to remove nonmeteor echoes, such that only pulsations in a narrow frequency band were accounted. Because of this, the occurrence rate of pulsating PMSE is biased by the software and cannot be treated as an occurrence rate of pulsating aurora.

The proposed mechanism is able to explain all observational features of pulsating PMSE. Unfortunately, auroral observations during the polar summer are impossible because of the sunlight sky, and therefore a direct confirmation of the proposed hypothesis of auroral pulsations is hardly possible. Signatures of pulsating aurora could be obtained from satellite data of precipitating electrons, but a probability of collocated satellite observations is very low.

Fortunately, some signatures of pulsating precipitation may be inferred from the SGO ionosonde data. For instance, the ionogram presented in Figure 7 shows a trace at 82 km, which is reflection from this height of radio waves at frequencies up to 5 MHz, at least. The trace is not continuous exhibiting irregular changes of the power of reflection as a function of the frequency. The SGO ionosonde is a frequency modulated continuous wave chirp sounder (Enell et al., 2016), which transmits a continuous 30-s signal with linearly increasing frequency from 0.5 to 16 MHz, at a rate of the frequency increase 0.5 MHz s^{-1} . Due to this the horizontal (frequency) axis in Figure 7 may be interpreted as a time axis where 1 s corresponds to 0.5 MHz. In such a case, the power changes may be considered as signatures of time variations of the auroral absorption caused by pulsating precipitation of electrons. The time variations are on the subsecond scale, which agree with pulsating auroral precipitation during the event of pulsating PMSE. Thus, the ionosonde may be used to confirm the proposed hypothesis, but future studies with a rigorous analysis of the ionosonde data are required.

5. Summary

In the summer time (late June–July), the high latitude SGO meteor radar (around 67°N) operating at a frequency of 36.9 MHz detected near-zenith echoes at elevation higher than 83° . The echoes were received from a narrow interval of altitudes near 82 km, which corresponds to the altitude of noctilucent clouds. The amplitude of the echoes showed irregular variations at a frequency of the order of a few Hz, so that we classified these echoes as pulsating PMSE. The pulsating PMSE were observed as events lasting about 1–2 h when >10 near-zenith echoes per an hour were detected. During 11 years, 2009–2019, 12 such events were recorded. The echoes occurred in the morning sector (4–12 MLT) during geomagnetic disturbances, when the SGO ionosonde showed electron density of the order of $3 \times 10^{11} \text{ m}^{-3}$ around 82 km, and enhanced D-region ionization was manifested in the data of cosmic noise absorption.

To explain the pulsating PMSE, we propose that pulsating auroral precipitation can modulate the power of PMSE at the subsecond time scale. In more detail, the proposed mechanism can be described as below.

Pulsating precipitation corresponding to the internal modulation can be represented as short (0.2–0.5 s) periodically repeating bursts of 50–100 keV electrons precipitating to the height of NLC where ice particles of about 50-nm radii exist. In response to the precipitation, the ice particles may quickly accumulate additional electrons due to the presence of hyperthermal electrons, according to the hypothesis proposed by Rosenberg et al. (2012). Smaller particles accumulate fewer electrons.

When the precipitation burst is ended, the ice particles carry excess electrons attached during the precipitation burst, which leads to PMSE backscatter that is larger than before the precipitation burst. After that the ice particles lose their excessive charge due to attractive interaction with ions.

For the 50-nm ice particles, the characteristic times of all considered processes are <0.2 s. Thus, we obtain variations of the amplitude of PMSE backscatter at the subsecond scale, which is erroneously recorded by the meteor radar as a meteor trail.

For the SKiYMET detection of pulsating PMSE, a coincidence of specific conditions is required, namely large 50-nm ice particles in the mesosphere, few-Hz pulsating auroral precipitation, energy of precipitating electrons 50–100 keV, and flux of the electrons in certain range to produce D-region ionization of the order of $(2\text{--}4) \times 10^{11} \text{ m}^{-3}$. These conditions are only met during the summer and during active magnetic conditions, and hence they are rare.

Appendix A: Electric Charge of Ice Particles at NLC Altitudes

The pulsating PMSE were obtained from the height around 82 km, which corresponds to the altitude of NLC where the largest ice particles (~ 50 nm in radii) exist (e.g., von Cossart et al., 1999).

The ice particles (aerosol grains) are charged due to microscopic currents of electrons and ions of the ambient plasma onto the grain surface and their attachment and recombination there (Fortov et al., 2006). Below we estimate the charge (Z_a) acquired by the ice particles at the height around 82 km. At this height for a grain of selected size (r_a), the Debye length (r_D), and the collision free path of ions (electrons) ($l_{i(e)}$), the following condition is satisfied:

$$r_a \ll r_D \ll l_{i(e)} \quad (\text{A1})$$

Under these conditions, the orbit motion limited theory is applicable and the following equation is derived from the equality of the electron and ion fluxes recombining on the grain surface (Fortov et al., 2006)

$$\exp(-z) = \frac{n_i}{n_e} \left(\frac{\mu}{\theta} \right)^{1/2} (1 + z\theta) \quad (\text{A2})$$

where $z = |Z_{a0}|e^2/4\pi\epsilon_0 r_a k T_e$, $\theta = T_e/T_i$, and $T_{i(e)}$ and $m_{i(e)}$ are the temperature and mass of ions (electrons), e is the electron charge, ϵ_0 is the permittivity of space, k is Boltzmann's constant. Solving Equation A2 for an isolated grain in a quasineutral plasma ($n_i = n_e$) and typical lower ionospheric conditions ($\theta = 1$ and $m_i \approx 50m_u$, where m_u is the atomic mass unit) we obtain $z \approx 4.1$. This gives for a grain of 50-nm radius in cold summer mesosphere ($T_i \approx T_e \approx 150$ K) a typical grain charge of the order of $Z_{a0} \approx 2$ elementary charge units.

According to the hypothesis proposed by Rosenberg et al. (2012), additional electrons may be attached to the ice particles during auroral precipitation. This charging process is initiated by dissipation of high-energy electrons during auroral activity producing a population of hyperthermal secondary electrons, such that a bump in the tail of the electron distribution between about 2.2 and 4.5 eV may appear due to small cross sections in that energy range for the vibrational and electronic excitation of N_2 and O_2 . According to the model developed by Rosenberg et al. (2012), if the density n_h of hyperthermal electrons with an energy $E_h \approx 3.5$ eV is about 0.03 of the total electron density n_e , 50-nm aerosol particles may attach up to $|Z_a| \approx 4$ electrons, and the electron attachment time is given by

$$\tau_{att} = \left(s_h n_h V_h \pi r_a^2 \left(1 - \frac{|Z_a| e^2}{4\pi\epsilon_0 E_h r_a} \right) \right)^{-1} \quad (\text{A3})$$

where $s_h \approx 1$ is the electron sticking coefficient and $n_h V_h$ is the hyperthermal electron flow ($E_h = m_e V_h^2/2$). In particular, for the typical values given above and $n_e \approx 3 \times 10^{11} \text{ m}^{-3}$, the time constant is 0.01 s.

The population of hyperthermal electrons may exist while the auroral precipitation is ongoing. After the precipitation is ended, the electrons are thermalized due to electron-neutral collisions. The frequency of electron-neutral collisions can be estimated as $\nu_{en} = 5.4 \cdot 10^{-10} n_n T_e^{1/2}$ (Kelley, 2009), which gives a value $2.7 \times 10^6 \text{ s}^{-1}$ at the height 82 km where the density of the neutral atmosphere, n_n , is $4 \times 10^{14} \text{ m}^{-3}$ according to the MSIS E-90 model (Hedin, 1991) and $T_e = 150$ K. The time of thermalization is given by

$$\tau_{th} = (\delta_{en} \nu_{en})^{-1} \quad (\text{A4})$$

where δ_{en} is the fraction of energy which an electron loses in one collision. For elastic collisions $\delta_{en} = 2m_e/m_n$ which gives $\tau_{th} \approx 0.01$ s (with the mass of neutral molecules $m_n \approx 30m_u$). In the case of nonelastic collisions, the time of electron thermalization is much <0.01 s.

After the hyperthermal electrons have been thermalized, the ice particles start to lose their excessive charge. The fastest process leading to deionization of the ice particles in the D-region is attractive interaction with ions. According to the theory developed by Natanson (1960), the attraction time is given by

$$\tau_{atr} = \left(n_i \pi r_a^2 v_i \left(1 + \frac{|Z_a| e^2}{4\pi\epsilon_0 k T_i r_a} \right) \right)^{-1} \quad (\text{A5})$$

where v_i is the mean thermal velocity of the ions, $T_i \approx 150$ K is the ion temperature which is taken equal for all charged and neutral components, and n_i is the ion density. In particular, for 50-nm particles, $m_i \approx 50m_u$, and $n_i \approx 3 \times 10^{11} \text{ m}^{-3}$, the time constant is about 0.2 s.

Data Availability Statement

The meteor radar data were collected at SGO (<https://www.sgo.fi/Projects/SLICE/>). Data used in the paper are available online (at https://www.sgo.fi/pub/JGR_PMSE_2020). The SGO ionosonde and CNA data are available at <https://www.sgo.fi/Data/archive.php>. The OMNI data were obtained from the GSFC/SPDF OMNIWeb interface at <https://omniweb.gsfc.nasa.gov>. The ESRAD data are available at <http://www2.irf.se//program/paf/mst/>.

Acknowledgments

S. Shalimov acknowledges support from the Academy of Finland via Grant 322360. M. Lester acknowledges support by STFC Grant ST/S000429/1.

References

- Chau, J. L., Strelnikova, I., Schult, C., Oppenheim, M. M., Kelley, M. C., Stober, G., & Singer, W. (2014). Nonspecular meteor trails from non-field-aligned irregularities: Can they be explained by presence of charged meteor dust? *Geophysical Research Letters*, *41*, 3336–3343. <https://doi.org/10.1002/2014GL059922>
- Chilson, P., Kirkwood, S., & Nilsson, A. (1999). The Esrange MST radar: A brief introduction and procedure for range validation using balloons. *Radio Science*, *34*, 427–436. <https://doi.org/10.1029/1998RS900023>
- Enell, C.-F., Kozlovsky, A., Turunen, T., Ulich, T., Väitalo, S., Scotto, C., & Pezzopane, M. (2016). Comparison between manual scaling and Autoscala automatic scaling applied to Sodankylä Geophysical Observatory ionograms. *Geoscientific Instrumentation, Methods and Data Systems*, *5*, 53–64. <https://doi.org/10.5194/gi-5-53-2016>
- Fortov, V. E., Iakubov, I., & Khrapak, A. (2006). *Physics of strongly coupled plasma* (p. 520). Oxford University Press.
- Grandin, M., Aikio, A. T., & Kozlovsky, A. (2019). Properties and geoeffectiveness of solar wind high-speed streams and stream interaction regions during solar cycles 23 and 24. *Journal of Geophysical Research: Space Physics*, *124*, 3871–3892. <https://doi.org/10.1029/2018JA026396>
- Gudadze, N., Stober, G., & Chau, J. L. (2019). Can VHF radars at polar latitudes measure mean vertical winds in the presence of PMSE? *Atmospheric Chemistry and Physics*, *19*(7), 4485–4497. <https://doi.org/10.5194/acp-19-4485-2019>
- Hall, C., Adami, C., Tsutsumi, M., & Carley, J. (2020). First observations of polar mesospheric echoes at both 31 MHz and 53.5 MHz over Svalbard (78.2 N 15.1 E). *Experimental Results*, *1*, e44. <https://doi.org/10.1017/exp.2020.51>
- Hedin, A. E. (1991). Extension of the MSIS thermosphere model into the middle and lower atmosphere. *Journal of Geophysical Research*, *96*, 1159–1172. <https://doi.org/10.1029/90JA02125>
- Hocking, W. K., Fuller, B., & Vandeppeer, B. (2001). Real-time determination of meteor-related parameters utilizing modern digital technology. *Journal of Atmospheric and Solar-Terrestrial Physics*, *63*, 155–169. [https://doi.org/10.1016/S1364-6826\(00\)00138-3](https://doi.org/10.1016/S1364-6826(00)00138-3)
- Kaifler, N., Kaifler, B., Wilms, H., Rapp, M., Stober, G., & Jacobi, C. (2018). Mesospheric temperature during the extreme midlatitude noctilucent cloud event on 18/19 July 2016. *Journal of Geophysical Research: Atmospheres*, *123*, 13775–13789. <https://doi.org/10.1029/2018JD029717>
- Kelley, M. C. (2009). *The Earth's ionosphere: Plasma physics and electrodynamics* (2nd ed., p. 536). Elsevier.
- King, J. H., & Papitashvili, N. E. (2005). Solar wind spatial scales in and comparisons of hourly Wind and ACE plasma and magnetic field data. *Journal of Geophysical Research*, *110*, A02104. <https://doi.org/10.1029/2004JA010649>
- Kozlovsky, A., Lukianova, R., & Lester, M. (2020). Occurrence and altitude of the long-lived nonspecular meteor trails during meteor showers at high latitudes. *Journal of Geophysical Research: Space Physics*, *125*, e2019JA027746. <https://doi.org/10.1029/2019JA027746>
- Kozlovsky, A., Shalimov, S., Kero, J., Raita, T., & Lester, M. (2018). Multi-instrumental observations of nonunderdense meteor trails. *Journal of Geophysical Research: Space Physics*, *123*, 5974–5989. <https://doi.org/10.1029/2018JA025405>
- Kozlovsky, A., Shalimov, S., & Lester, M. (2017). Mesospheric plasma irregularities caused by the missile destruction on 9 December 2009. *Journal of Geophysical Research: Space Physics*, *122*, 6696–6707. <https://doi.org/10.1002/2017JA024300>
- Kozlovsky, A., Shalimov, S., Oyama, S., Hosokawa, K., Lester, M., Ogawa, Y., & Hall, C. (2019). Ground echoes observed by the meteor radar and high-speed auroral observations in the substorm growth phase. *Journal of Geophysical Research: Space Physics*, *124*, 9278–9292. <https://doi.org/10.1029/2019JA026829>
- Kvitte, G. J., & Pettersen, H. (1969). Morphology of the pulsating aurora. *Planetary and Space Science*, *17*, 1599–1607. [https://doi.org/10.1016/0032-0633\(69\)90148-2](https://doi.org/10.1016/0032-0633(69)90148-2)
- Lukianova, R., Kozlovsky, A., & Lester, M. (2018). Climatology and inter-annual variability of the polar mesospheric winds inferred from meteor radar observations over Sodankylä (67N, 26E) during solar cycle 24. *Journal of Atmospheric and Solar-Terrestrial Physics*, *171*, 241–249. <https://doi.org/10.1016/j.jastp.2017.06.005>

- Miyoshi, Y., Oyama, S., Saito, S., Kurita, S., Fujiwara, H., Kataoka, R., et al. (2015). Energetic electron precipitation associated with pulsating aurora: EISCAT and Van Allen Probe observations. *Journal of Geophysical Research: Space Physics*, *120*, 2754–2766. <https://doi.org/10.1002/2014JA020690>
- Natanson, G. L. (1960). On the theory of the charging of amicroscopic aerosol particles as a result of capture of gas ions. *Soviet Physics-Technical Physics*, *5*, 538–551 (English Translation).
- Nishiyama, T., Sakanoi, T., Miyoshi, Y., Hampton, D. L., Katoh, Y., Kataoka, R., & Okano, S. (2014). Multiscale temporal variations of pulsating auroras: On-off pulsation and a few Hz modulation. *Journal of Geophysical Research: Space Physics*, *119*, 3514–3527. <https://doi.org/10.1002/2014JA019818>
- Rapp, M., & Lübken, F.-J. (2004). Polar mesosphere summer echoes (PMSE): Review of observations and current understanding. *Atmospheric Chemistry and Physics*, *4*, 2601–2633. <https://doi.org/10.5194/acp-4-2601-2004>
- Rees, M. H. (1963). Auroral ionization and excitation by incident energetic electrons. *Planetary and Space Science*, *11*, 1209–1218. [https://doi.org/10.1016/0032-0633\(63\)90252-6](https://doi.org/10.1016/0032-0633(63)90252-6)
- Reid, G. C. (1975). Ice clouds at the summer polar mesopause. *Journal of the Atmospheric Sciences*, *32*(3), 523–535. [https://doi.org/10.1175/1520-0469\(1975\)032<0523:ICATSP>2.0.CO;2](https://doi.org/10.1175/1520-0469(1975)032<0523:ICATSP>2.0.CO;2)
- Richardson, I. G., & Cane, H. V. (2010). Near-Earth interplanetary coronal mass ejections during solar cycle 23 (1996–2009): Catalog and summary of properties. *Solar Physics*, *264*, 189–237. <https://doi.org/10.1007/s11207-010-9568-6>
- Rosenberg, M., Varney, R. H., Kelley, M. C., & Paschall, D. (2012). Possible effect of hyperthermal electrons on the charging of mesospheric dust. *Journal of Atmospheric and Solar-Terrestrial Physics*, *74*, 124–128. <https://doi.org/10.1016/j.jastp.2011.10.011>
- Smirnova, M., Belova, E., Kirkwood, S., & Mitchell, N. (2010). Polar mesosphere summer echoes with ESRAD, Kiruna, Sweden: Variations and trends over 1997–2008. *Journal of Atmospheric and Solar-Terrestrial Physics*, *72*, 435–447. <https://doi.org/10.1016/j.jastp.2009.12.014>
- Sommer, S., Chau, J. L., & Schult, C. (2016). On high time-range resolution observations of PMSE: Statistical characteristics. *Journal of Geophysical Research: Atmospheres*, *121*, 6713–6722. <https://doi.org/10.1002/2015JD024531>
- Swarnalingam, N., Hocking, W. K., Singer, W., & Latteck, R. (2009). Calibrated measurements of PMSE strengths at three different locations observed with SKIYMET radars and narrow beam VHF radars. *Journal of Atmospheric and Solar-Terrestrial Physics*, *71*, 1807–1813. <https://doi.org/10.1016/j.jastp.2009.06.014>
- von Cossart, G., Fiedler, J., & von Zahn, U. (1999). Size distributions of NLC particles as determined from 3-color observations of NLC by ground-based lidar. *Geophysical Research Letters*, *26*, 1513–1516. <https://doi.org/10.1029/1999GL900226>
- Younger, J. P., Reid, I. M., Adami, C. L., Hall, C. M., & Tsutsumi, M. (2021). Meteor radar observations of polar mesospheric summer echoes over Svalbard. *Atmospheric Measurement Techniques*, *14*, 5015–5027. <https://doi.org/10.5194/amt-14-5015-2021>